IEEE Access
Multidisciplinary | Rapid Review | Open Access Journal

Received 9 November 2022, accepted 25 November 2022, date of publication 1 December 2022,
date of current version 9 December 2022.

Digital Object Identifier 10.1109/ACCESS.2022.3226331

RESEARCH ARTICLE

MRWM: A Multiple Residual Wasserstein Driven Model for Image Denoising

RUI-QIANG HE, WANG-SEN LAN, AND FANG LIU
Department of Mathematics, Xinzhou Teachers University, Xinzhou 034000, China
Corresponding author: Rui-Qiang He (ruiqianghe@sina.com)

This work was supported in part by the National Natural Science Foundation of China under Grant 61772389.

ABSTRACT Residual histograms can provide valuable information for vision research. However, current image restoration methods have not fully exploited the potential of multiple residual histograms, especially their role as overall regularization constraints. In this paper, we propose a novel framework of multiple residual Wasserstein driven model (MRWM) that can organically combine multiple residual Wasserstein constraints and various natural image priors for image denoising. Specifically, by utilizing the Wasserstein distance derived from the optimal transmission theory, the multiple residual histograms of the observed images are forced to be as close as possible to the reference residual histogram, thereby improving the accuracy of residual estimation. Furthermore, the proposed concrete MRWM unifies the multiple residual Wasserstein distribution approximation and the image total variation prior knowledge to carry out image denoising. Alternating iterative algorithm of histogram matching and Chambolle dual projection has the characteristics of less parameters and easy implementation. Finally, our experiments confirm that compared with some representative image denoising algorithms, the MRWM can obtain better performance in objective evaluation, and can better preserve the details such as the image edges, making the image look more natural.

INDEX TERMS Wasserstein distance, multiple residual, histogram matching, image denoising.

I. INTRODUCTION

Image denoising, which aims to reconstruct a potential clean image x from a noisy degraded image y, is one of the classic but still active low-level vision research tasks [1], [2], [3], [4], [5], [6], [7], [8], [9]. A widely used data model is $y = x + n$, where n is additive white Gaussian noise. At present, methods on image denoising can be divided into two categories: model-based methods and deep learning-based methods. The first class of methods often estimates clean image by mining various image priors, while the second one mainly employs neural networks to learn a mapping from noisy image to clean image [5], [6], [10], [11]. Here we briefly describe these two classes of image denoising methods respectively.

A. MODEL-BASED METHODS

Due to the fact that the gradients of natural images have heavy-tailed distributions, sparse priors are widely applied to image denoising [12]. Sparse coding has been shown to be effective in image denoising by representing image patches as sparse linear combinations of atoms in an over-complete dictionary [13]. Later, by using superpixel segmentation, SSLRR [14] presents a low-rank approximation image denoising method. A local low-rank image denoising method via tensor decomposition [15] is introduced. By utilizing intra and inter patch correlation, LIIC [16] shows an image denoising method with low-rank regularization. SLG [17] proposes a structure-based low-rank model for noise removal. SLG exploits manifold structure information to embed graph kernel norm regularization into a low-rank approximation model. The weighted singular-value thresholding algorithm solves the model effectively and achieves excellent denoising performance.

As one of the milestones in the history of image denoising, BM3D [18] fully explores the nonlocal self-similarity (NSS) of natural images. The combined use of NSS and sparse priors has resulted in some outstanding work [12], [19], [20]. By forcing the gradient histogram of the denoised image to

The associate editor coordinating the review of this manuscript and approving it for publication was Huaqing Li.

be as close as possible to the reference gradient histogram of the clean image, GHP [21] presents a texture-enhanced image denoising algorithm. Based on the information that in some practical problems singular values have clear physical meaning and should be treated differently, WNNM [22] applied to image restoration studies the weighted kernel norm minimization problem, in which different singular values can be weights adaptively.

Recently, ATVBH [23] presents a higher-order TV image restoration method by combining first-order and second-order total variations with adaptive parameter estimation. CAS [24] fully utilizes local and non-local correlation of natural image contents, respectively, to achieve near-optimal sparse representations that minimize signal uncertainty. For highly correlated image data groups, CAS employs a content-adaptive transform to obtain the sparsest representation, thereby resulting in outstanding denoising performance. By combining a thresholding function and image TV regularization, a modified TV regularization method M-TVRM [25] is proposed for salt and pepper noise (SPN) removal. The thresholding function based on SPN characteristics is utilized for noise pixel detection, and the image TV regularization is employed to restore the noisy pixels.

By mining the fact that many natural images have low-dimensional block manifold structure [26], [27], [28], [29], LDMM [1] and G-LDMM [30] are applied to image denoising and inpainting by point integral method and weighted non-local Laplacian(WNLL), respectively. The combination of low-dimensional manifold and residual distribution approximation produces W-LDMM [31], which is well applied to natural image restoration. It can be seen that various image prior information plays an important role in these methods.

B. DEEP LEARNING-BASED METHODS

In recent years, image denoising methods based on deep learning have been widely developed. Deep convolutional neural networks have achieved great success in low-level visual tasks including image denoising [32], [33], [34]. An improved encoder-decoder network [35] is constructed for image denoising by utilizing symmetric skip connections. By adding batch normalization to the residual learning framework, DnCNN [36] builds image denoising networks that perform significantly better than traditional denoising algorithms. To enable memory of the network, a densely connected denoising neural network [37] is constructed.

After these, a convolutional neural network based on multilevel wavelet denoising [38] is proposed. A fast and flexible network FFDNet [39] is put forward to process images with nonuniform noise. By solving the fractional optimal control problem, FOCNet [6] develops an advanced Gaussian denoising neural network. Employing graph convolution operation, a neural network architecture is proposed to create neurons with non-local receptive fields for image denoising [40].

To deal with the problem that feature scaling in image denoising loses some visual informative details, AGSN [41] presents a fast and accurate image denoising method by attention guided scaling network. By utilizing the attention guided adversarial training, AGSN enhance the reconstruction quality of the images with challenging noisy texture. In DER-Net [42], a multilevel network that efficiently utilizes GPU memory is proposed for biological-image denoising. DER-Net, which is composed of U-Net encoder-decoder structures, has a strong ability to recover the details of biological images. It can be found that these deep learning methods obtain excellent image denoising performance, but also need to pay a high computational cost under the powerful hardware platform.

C. MOTIVATION

With the continuous improvement of modern imaging technology, multiple images with the same content can be obtained almost instantaneously on one imaging device. For example, a mobile phone can take dozens of images in a second, while a high-speed camera can take a larger number of images in an instant. But these images in the acquisition, transmission, storage, processing links sometimes inevitably encounter noise pollution. Therefore, denoising multiple noisy images is a realistic and meaningful research topic. One can consider estimating a latent clean image x from multiple noisy image data $\{y_\mu, \mu = 1, 2, \cdots, M\}$ acquired in an instant from an imaging facility. Here M is the number of contaminated images. In other words, the observed versions of the multiple noisy images can be defined as the following formula:

$$y_\mu = x + n_\mu, \quad \mu = 1, 2, \cdots, M, \tag{1}$$

where n_μ is additive white Gaussian noise with mean zero and standard deviation σ. As in the literatures [43], [44], the noise standard deviation σ can be estimated from multiple noisy images through the finest scale wavelet coefficients and median filtering.

Different from the most image restoration methods that focus on mining the prior information of images, the multiple residual Wasserstein driver model (MRWM) proposed in this paper is designed primarily to regularize the multiple residual images $n_\mu = y_\mu - x$, $(\mu = 1, 2, \cdots, M)$, i.e., the differences between the degraded images y_μ and the potential image x.

Although the Gaussian noises contained in the images are random, their distribution is clear. Therefore, we can make full use of the Wasserstein distance to make the estimated residual histograms as close as possible to the reference Gaussian noise histogram, so as to improve the residual estimation accuracy. As we know, the training of the GAN based denoising network [45], [46], [47] is to minimize the weighted sum of the content loss and adversarial loss. However, the proposed MRWM is a model based image denoising method which ably combines the multiple residual Wasserstein constraints and image prior regularization. The key idea of MRWM is to reduce the difference between the estimated residual histograms and the reference Gaussian

noise histogram through the multiple residual Wasserstein distance.

D. CONTRIBUTION

The contributions of this paper can be summarized as follows: (1) A novel unified framework of multiple residual Wasserstein driven model (MRWM) is proposed. The framework can effectively combine the multiple residual Wasserstein distribution approximation with the existing image priors to perform image denoising. (2) A specific MRWM is constructed to combine multiple residual Wasserstein distance and classic image total variation prior to improve the quality of denoised images. (3) The proposed alternate iterative algorithm of histogram matching and Chambolle dual projection has the characteristics of fewer parameters and easy implementation, and achieves excellent image denoising performance.

The rest of this paper is structured as follows. Section II introduces the basics of Wasserstein distance. Section III presents the unified framework of multiple residual Wasserstein driven model. Section IV proposes a specific multiple residual Wasserstein driven model. In Section V, we show the model solution process and algorithm design. Numerical experimental results are given in Section VI. Finally, Section VII concludes this paper.

II. PRELIMINARIES ON WASSERSTEIN DISTANCE

The Wasserstein distance originated from the optimal transport theory is an effective tool to measure the difference between two histograms. The Wasserstein distance can be defined as the least cost which must be paid to convert one histogram to another. For the two known probability distributions p and q which are defined on the real number field R, the Wasserstein distance of p and q is expressed as the solution to the Monge problem [48]:

$$W(p,q) = \inf_{\phi} \int_{-\infty}^{\infty} (x-\phi(x))^2 p(x)dx, \tag{2}$$

where the random variable x follows the distribution p, while another variable $\phi(x)$ obeys the distribution q. The infimum in above Eq. (2) is for all the determined functions $\phi : R \mapsto R$ which map any random variable x to the variable $\phi(x)$. It can be seen that the Wasserstein distance is a statistical metric between two known probability distributions, and will go to zero if and only if p and q are the same distribution.

For a probability distribution p on R, its cumulative distribution function can be defined as $F_p(x) = \int_{-\infty}^{x} p(\tau)d\tau$, where F is called the histogram equalization transform [49]. Moreover, the percentile function of this probability distribution p is expressed as $F_p^{-1}(t) = \inf\{x \in R : F_p(x) > t\}$. In the comprehensive introduction part of the optimal transport theory [48], a fundamental conclusion is that the optimal ϕ in the problem (2) has the explicit closed-form solution:

$$\phi_{p\to q}(x) = F_q^{-1}(F_p(x)). \tag{3}$$

Since Monge problem (2) is actually an expected value, the Wasserstein distance can be further expressed as

$$W(p,q) = \inf_{\phi} E(x-\phi(x))^2. \tag{4}$$

By treating $x = (x_1, x_2, \cdots, x_n)^T$ as n independent samples stemed from the distribution p, and representing histogram h_q as the discrete approximation of the distribution q, the equivalent discrete definition of the Wasserstein distance can be introduced as follows:

$$\hat{W}(p,q) = \hat{W}(h_x, h_q) = \min_{\hat{\phi}} \frac{1}{n}\sum_{i=1}^{n}(x_i-\xi_i)^2, \tag{5}$$

where the function $\hat{\phi}$ converts x_i to $\xi_i = \hat{\phi}(x_i)$, such that the transformed samples $\xi = (\xi_1, \xi_2, \cdots, \xi_n)^T$ can satisfy the histogram h_q. Similar to the continuous case above, the optimal $\hat{\phi}$ for Eq. (5) also acquires a closed-form solution [48]:

$$\xi_i = \hat{\phi}_{h_x\to h_q}(x_i) = F_{h_q}^{-1}(F_{h_x}(x_i)), \tag{6}$$

where the cumulative distribution function F_{h_x} and the percentile function $F_{h_q}^{-1}$ are derived from the histograms h_x and h_q respectively.

If x is an image, then $\hat{\phi}$ is a histogram matching operator which can be applied to moving object detection and image contrast enhancement. For a known image $x = (x_1, x_2, \cdots, x_n)^T$, $\hat{\phi}$ ensures that the output sample $\xi = (\xi_1, \xi_2, \cdots, \xi_n)^T$ can match the given histogram h_q. Eqs. (5) and (6) constitute the theoretical basis of the proposed image denoising model in this paper.

III. THE UNIFIED FRAMEWORK OF MULTIPLE RESIDUAL WASSERSTEIN DRIVEN MODEL

Instead of regularizing only image prior information in most image restoration models, the proposed model is designed to mainly regularize residual images $n_\mu = y_\mu - x, (\mu = 1, 2, \cdots, M)$, i. e., the differences between the noisy observations and the potential clean image.

We know that for each noisy sample image, its residual $y_\mu - x$ should theoretically obey the Gaussian distribution. We make full use of the Wasserstein distance distribution approximation effect to make each residual histogram $h_{y_\mu - x}, (\mu = 1, 2, \cdots, M)$ as close as possible to the reference Gaussian noise histogram (ground truth) h_g. Based on these, we propose the following unified framework of multiple residual Wasserstein driven model (MRWM) for image denoising:

$$\arg\min_{x} R(x) + \sum_{\mu=1}^{M} \frac{\beta_\mu}{2}\hat{W}(h_{y_\mu - x}, h_g), \tag{7}$$

where the first term $R(x)$ represents prior knowledge about the original clean image x. $\hat{W}(h_{y_\mu - x}, h_g)$ is the Wasserstein distance between $h_{y_\mu - x}$ and h_g. Here β_μ is the Wasserstein scale parameter.

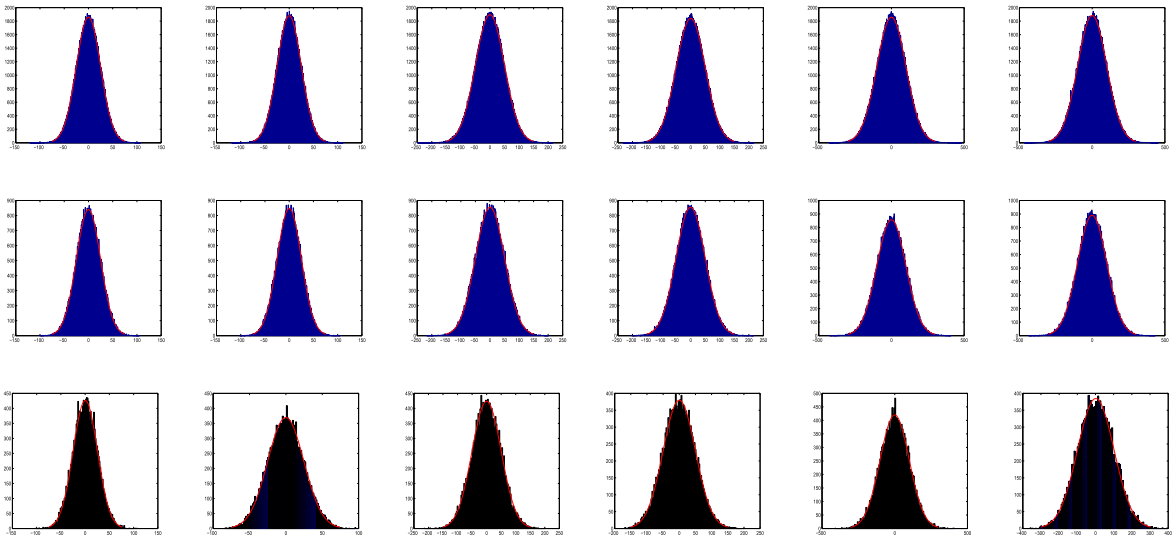

FIGURE 1. The stability analysis of the reference Gaussian noise histogram is carried out in terms of pixel size and noise level. From the first to third rows, they are randomly generated histograms of Gaussian noise with pixel sizes of 512 × 512, 256 × 256, 128 × 128, respectively. In the histograms of the first two columns, the middle two ones, and the last two ones, the corresponding Gaussian noise standard deviations are 25, 50, and 100, respectively. It can be found that the stability of the noise histogram is mainly affected by the pixel size rather than the noise level.

The Eq. (7) above is an organic combination of image prior regularization and multiple residual Wasserstein distance constraints. Popular $R(x)$ includes the probability models of image patches [13], [50], the heavy-tail distribution models in the gradient domain [51], [52], and the low-dimensional manifold prior models in most of the natural images [1], [31]. One can see that the existing image priors can be easily embedded into the framework (7) for image denoising.

IV. A SPECIFIC MULTIPLE RESIDUAL WASSERSTEIN DRIVEN MODEL

A. THE PROPOSED MRWM

Without loss of generality, in this paper, we choose the classic image total variation (TV) prior regularization and triple residual Wasserstein distance constrains ($M = 3$) to expound the effectiveness of the proposed MRWM framework. Therefore we mainly focus on the following specific multiple residual Wasserstein driven model (MRWM) for image denoising:

$$\arg\min_{x} \|\nabla x\|_1 + \frac{\beta_1}{2}\hat{W}(h_{y_1-x}, h_g) + \frac{\beta_2}{2}\hat{W}(h_{y_2-x}, h_g) + \frac{\beta_3}{2}\hat{W}(h_{y_3-x}, h_g), \quad (8)$$

where ∇x denotes the discrete gradient of the clean image, and $\|\nabla x\|_1$ represents the sum of the length of the gradient vector at each point.

In model (8), Wasserstein distance drives the estimated residual histogram to approximate the reference residual histogram, thus improving the residual estimation performance. The dual combination of Wasserstein multiple residual distribution approximation and image TV prior can improve the performance of image restoration. Subsequently, the stability of the reference Gaussian noise histogram h_g is analyzed. After that, we carry out the solution of the MRWM and the corresponding numerical experiments.

B. THE STABILITY ANALYSIS OF THE REFERENCE GAUSSIAN NOISE HISTOGRAM

Here, we analyze the stability of the reference Gaussian noise histogram h_g from the visual and numerical perspectives, respectively. Firstly, due to space factor, we present only 18 randomly generated Gaussian noise histograms in Figure 1. Concretely, the histograms shown in the three rows are derived from Gaussian noises which pixel sizes are 512×512, 256×256 and 128×128,respectively. The histograms in the first two columns, the middle two ones, and the last two ones, correspond to Gaussian noises with $\sigma = 25$, $\sigma = 50$, $\sigma = 100$, respectively. It can be found from Figure 1 that the first two rows of histograms have better stability, while the third row histograms are less stable. This implies that the stability of the reference Gaussian noise histogram is mainly affected by the size of the noise (image) pixels, rather than the noise level. In fact, the larger histogram contains more random sampling points, which helps to improve the stability of the histogram.

Then, the stability of reference noise histogram is analyzed numerically. Figure 2 presents the histograms of ten randomly generated Gaussian noises (512×512), which are all zero mean and $\sigma = 25$. The experimental results show that the average mean and standard deviation in the 10 histograms are -0.0035 and 25.0020, respectively. Meanwhile, the variance of this ten standard deviations is 2.6966×10^{-4}. Based on the above discussion, it can be concluded that the reference Gaussian noise histogram h_g in the model (8) is stable.

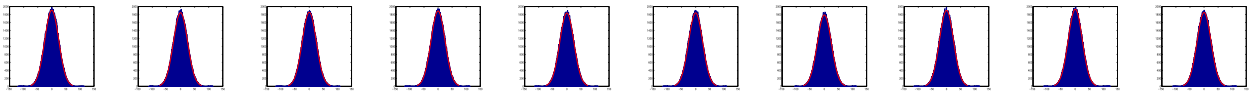

FIGURE 2. Ten randomly generated Gaussian noise histograms (512 × 512) with zero mean and $\sigma = 25$.

V. THE SOLUTION OF THE MULTIPLE RESIDUAL WASSERSTEIN DRIVEN MODEL

A. THE SOLUTION OF THE MRWM

The basic idea of solving the proposed MRWM (8) is to transform the problem with auxiliary variables and then carry out alternate iteration of variables.

First, three auxiliary variables ξ_1, ξ_2, ξ_3 are introduced, and the problem (8) is split into

$$\begin{aligned}\arg\min_{x,\xi_1,\xi_2,\xi_3} &\|\nabla x\|_1 + \frac{\beta_1}{2}\|\xi_1 - (y_1 - x)\|_2^2 \\ &+ \frac{\beta_2}{2}\|\xi_2 - (y_2 - x)\|_2^2 + \frac{\beta_3}{2}\|\xi_3 - (y_3 - x)\|_2^2 \\ s.t. &\, h_{\xi_1} = h_g, h_{\xi_2} = h_g, h_{\xi_3} = h_g. \end{aligned} \tag{9}$$

Next, By fixing x and ξ_1, ξ_2, ξ_3 (all three are fixed at the same time) respectively, the minimization problem (9) is solved. Specifically, when x in (9) is fixed, the following optimization problem need to be solved

$$\begin{aligned}\arg\min_{\xi_1,\xi_2,\xi_3} &\frac{\beta_1}{2}\|\xi_1 - (y_1 - x)\|_2^2 + \frac{\beta_2}{2}\|\xi_2 - (y_2 - x)\|_2^2 \\ &+ \frac{\beta_2}{2}\|\xi_3 - (y_3 - x)\|_2^2, \\ s.t. &\, h_{\xi_1} = h_g, h_{\xi_2} = h_g, h_{\xi_3} = h_g. \end{aligned} \tag{10}$$

The minimum point ξ_1, ξ_2, ξ_3 in (10) can be obtained by the histogram matching operation below,

$$(\xi_1)_i = \hat{\phi}_{h_{y_1-x}\to h_g}((y_1 - x)_i), \tag{11}$$

$$(\xi_2)_i = \hat{\phi}_{h_{y_2-x}\to h_g}((y_2 - x)_i), \tag{12}$$

$$(\xi_3)_i = \hat{\phi}_{h_{y_3-x}\to h_g}((y_3 - x)_i), \tag{13}$$

where the subscript i is the $i - th$ component. Here the histogram matching operator $\hat{\phi}$ can make the histograms of the outputs ξ_1, ξ_2, ξ_3 conform to the reference Gaussian noise histogram h_g.

On the other hand, when the variables ξ_1, ξ_2, ξ_3 are fixed, Eq. (9) changes to

$$\begin{aligned}\arg\min_{x} &\|\nabla x\|_1 + \frac{\beta_1}{2}\|\xi_1 - (y_1 - x)\|_2^2 \\ &+ \frac{\beta_2}{2}\|\xi_2 - (y_2 - x)\|_2^2 + \frac{\beta_3}{2}\|\xi_3 - (y_3 - x)\|_2^2. \end{aligned} \tag{14}$$

One can see that the last three quadratic terms in Eq. (14) can be combined into one term. So Eq. (14) reduces to

$$\arg\min_{x} \|\nabla x\|_1 + \frac{\beta_1 + \beta_2 + \beta_3}{2}\cdot \left\| \frac{\beta_1(y_1 - \xi_1) + \beta_2(y_2 - \xi_2) + \beta_3(y_3 - \xi_3)}{\beta_1 + \beta_2 + \beta_3} - x \right\|_2^2. \tag{15}$$

For simplicity of notation, let $\theta = \beta_1 + \beta_2 + \beta_3$, and

$$z = \frac{\beta_1(y_1 - \xi_1) + \beta_2(y_2 - \xi_2) + \beta_3(y_3 - \xi_3)}{\beta_1 + \beta_2 + \beta_3}.$$

Thus, Eq. (15) is simplified to

$$\hat{x} = \arg\min_{x} \|\nabla x\|_1 + \frac{\theta}{2}\|z - x\|_2^2. \tag{16}$$

It can be found that the above Eq. (16) is obviously a TV-L2 problem, which can be solved by the noted Chambolle duality projection algorithm [53]. In consequence, the solution of Eq. (16) is stated as follows

$$\hat{x} = z - \frac{divp}{\theta}, \tag{17}$$

where the vector p can be obtained by the following fixed point iteration method: initializing $p = 0$ and iterating

$$p = \frac{p + \tau\nabla(divp - \theta z)}{1 + \tau\,|\nabla(divp - \theta z)|}, \tag{18}$$

with $\tau \leq 1/8$ to ensure convergence, and readers can refer to [53] for more details here.

B. ALGORITHM DESIGN

To solve the proposed multiple residual Wasserstein-driven model, we design the above-mentioned optimization solution method, which can be summarized as Algorithm 1.

In essence, the algorithm is an alternate iterative implementation of histogram matching operation and Chambolle duality projection algorithm. Histogram matching makes the output residual more consistent with Gaussian distribution from the perspective of probability distribution, while Chambolle duality projection makes the output image more close to the original image. It can be seen that the algorithm is a process of implementing dual effects on residual distribution and output image.

VI. NUMERICAL EXPERIMENTS

In this section, the experimental parameters are first described. Then the experimental results on 12 test images and dataset BSD68 [54] are presented successively. Finally, the implementation efficiency of the experiment is analyzed.

A. PARAMETRIC DESCRIPTION

In the proposed MRWM (8), there are three model parameters β_1, β_2 and β_3. Considering that the status of the three noisy images is equal in the restoration process, we take three of

Algorithm 1 Multiple Residual Wasserstein Driven Model (MRWM) for Image Denoising

1. Initialize: $k = 1, x = eye(size(y_1))$.
2. Iterate on $k = 1, 2, \cdots, J$.
3. Update ξ_1, ξ_2, ξ_3 by the histogram matching operations:
$$(\xi_1)_i = \hat{\phi}_{h_{y_1-x}\to h_g}((y_1 - x)_i),$$
$$(\xi_2)_i = \hat{\phi}_{h_{y_2-x}\to h_g}((y_2 - x)_i),$$
$$(\xi_3)_i = \hat{\phi}_{h_{y_3-x}\to h_g}((y_3 - x)_i).$$
4. Update θ:
$$\theta = \beta_1 + \beta_2 + \beta_3.$$
5. Update z:
$$z = \frac{\beta_1(y_1 - \xi_1) + \beta_2(y_2 - \xi_2) + \beta_3(y_3 - \xi_3)}{\beta_1 + \beta_2 + \beta_3}.$$
6. Fixed-point iteration: initializing $p = 0$ and iterating
$$p = \frac{p + \tau\nabla(divp - \theta z)}{1 + \tau\,|\nabla(divp - \theta z)|}.$$
7. Implement Chambolle's duality projection:
$$\hat{x} = z - \frac{divp}{\theta}.$$
8. $k \leftarrow k + 1$

the same parameters, namely $\beta_1 = \beta_2 = \beta_3$. It is known that most model-based image restoration methods contain several model parameters. Finding optimal parameters by manual tuning is a daunting task. In fact, the MRWM has only one parameter, which makes the experiment easy to implement.

The general theory of setting regularization parameters in image restoration is to ensure that the solution obtained by the model satisfies the discrepancy principle. Specifically, adjusting the optimal parameter pursues to make the variances of the output residuals $y_\mu - x$, $(\mu = 1, 2, 3)$ equal to the noise variance σ^2 as much as possible. In the specific experiment process, we take the test image "plane" as an example to illustrate the change curve of PSNR with $\beta_i (i = 1, 2, 3)$. The curve are shown in the Figure 3. Combined with some experimental experience, we finally determine the optimal parameters $\beta_i = 0.82$, $(i = 1, 2, 3)$.

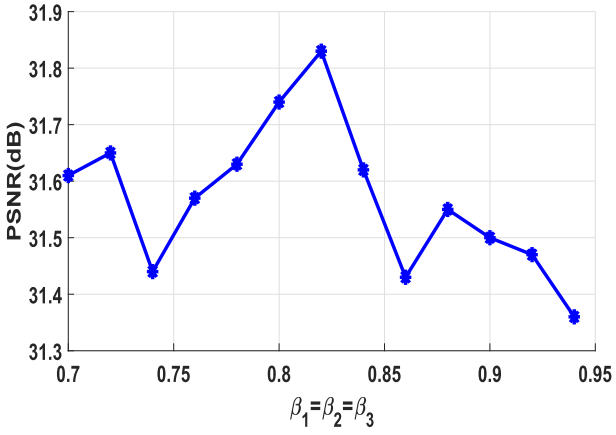

FIGURE 3. The graph of PSNR with $\beta_i (i = 1, 2, 3)$ in MRWM. It can be seen that the optimal model parameters $\beta_1 = \beta_2 = \beta_3 = 0.82$.

The initial iteration input x in Algorithm 1 is selected as the identity matrix of the same size as the noisy image. In experiments, we set the iteration number J=300. In fixed point iteration, the parameter $\tau = 1/8$, which can achieve convergence.

We employ the 12 test images shown in Figure 4 and the commonly used test dataset BSD68 [54] to illustrate the effectiveness of the MRWM. In the experiments, the images to be processed contain Gaussian noise with $\sigma = 25$. The experimental hardware platform is dual-core CPU (1.80 GHz and 2.30 GHz), 64.0 GB RAM. The operating system is Windows 10.0, and the software environment is Matlab R2017b.

B. EXPERIMENTAL RESULTS ON 12 TEST IMAGES

The experimental results on the 12 test images shown in Figure 4 consist of two parts: the comparison of multi-sample and single-sample experiments; the comparison of MRWM with several representative denoising methods.

Firstly, Table 1 displays the denoising result comparison of MRWM-1 (i.e. $\beta_1 = 0.82, \beta_2 = \beta_3 = 0$ in (8)), MRWM-2 (i.e. $\beta_1 = \beta_2 = 0.82, \beta_3 = 0$ in (8)), and MRWM-3 (i.e. $\beta_1 = \beta_2 = \beta_3 = 0.82$ in (8)). In order to investigate the case of denoising four images (namely $\mu = 4$ in Eq. (1)), we also add the corresponding experimental result MRWM-4 in Table 1. Figure 5 shows the PSNR and SSIM statistical figures of the three methods MRWM-1, MRWM-2 and MRWM-3. It can be seen that as the image sample number increases, PSNR and SSIM of the recovered images are significantly increased. In addition, Figure 6 illustrates the visual comparison of local magnification. It can be seen that increasing the number of image samples can significantly improve the visual performance of the restored image. These show that the proposed multiple residual histogram approximation by the Wasserstein distance is effective in image denoising.

Then, Table 2 shows the experimental results of MRWM and five representative Gaussian denoising methods BM3D [18], NCSR [20], GHP [21], WNNM [22], W-LDMM [31]. Fiugre 7 gives the average PSNR and SSIM curves of these six methods acting on 12 test images. One can see that MRWM is superior to the competing methods in terms of average PSNR and SSIM.

We know that the denoising effect of the classic TV-L2 is not as good as that of BM3D. However, from the experimental results in this paper, it can be found that the denoising effect of MRWM is better than that of the above representative denoising methods. In addition, in the specific experimental process, we also found that the effect of total variation is limited. This is because total variation is only a regularization of the image itself. For the problem of estimating the original image from multiple noisy images, multiple residual Wasserstein distance constraints can play a more important role.

In addition, the enlarged partial details of some images are shown in Figure 8 and Figure 9. As can be seen in Figure 8, compared to the original image, the fine particles around the starfish obtained by BM3D, NCSR, GHP, WNNM

FIGURE 4. Twelve test images for Gaussian denoising. From left to right and top to bottom, they are labeled 1 to 12, respectively.

TABLE 1. Gaussian denoising PSNR (dB) and SSIM comparison for MRWM-1, MRWM-2, MRWM-3 and MRWM-4 on the 12 test images shown in Figure 4.

Images	1	2	3	4	5	6	7	8	9	10	11	12	Avg.
MRWM-1	28.84	22.86	27.33	26.21	28.11	26.27	22.85	22.14	21.95	22.96	22.96	19.50	24.33
	0.7736	0.4640	0.6893	0.7664	0.8198	0.6871	0.5305	0.3823	0.5034	0.5665	0.3413	0.5047	0.5857
MRWM-2	30.06	28.33	28.82	27.15	30.09	27.00	25.87	27.23	26.85	27.24	26.50	23.17	27.36
	0.8311	0.7134	0.7711	0.8051	0.8599	0.7183	0.7340	0.6122	0.7390	0.7610	0.5733	0.5742	0.7244
MRWM-3	31.83	30.12	30.11	29.42	30.46	27.70	30.05	30.10	29.60	27.85	32.48	28.23	29.83
	0.8856	0.7842	0.8122	0.8698	0.8672	0.7420	0.8763	0.8200	0.8533	0.7812	0.8408	0.8055	0.8282
MRWM-4	32.32	30.33	31.11	29.00	30.88	28.86	30.46	30.62	29.64	28.47	32.96	28.81	30.29
	0.8874	0.7905	0.8408	0.8593	0.8780	0.7674	0.9159	0.7708	0.8443	0.8295	0.8362	0.8296	0.8375

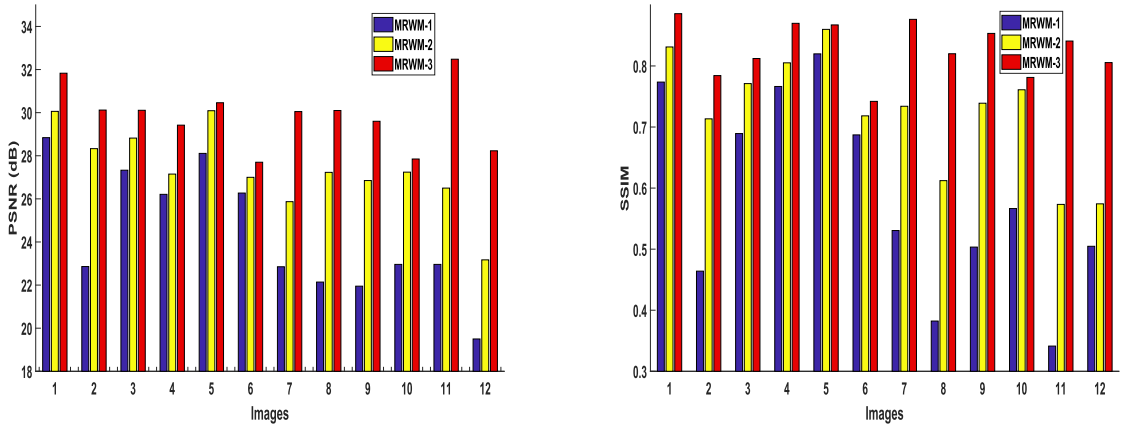

FIGURE 5. PSNR and SSIM result statistical figures of three denoising methods MRWM-1, MRWM-2 and MRWM-3 on 12 test images.

and W-LDMM are polished. However, the proposed MRWM can better preserve these details, which make the denoised images look more natural and visually pleasing. We can also find from Figure 9 that the competitive methods tend to over-smooth image edges. In contrast, MRWM retains sharper edge information, which is an important image detail feature.

The proposed MRWM is a denoising method, which mainly deals with gray images. However, with the help of YUV color space [55], [56], MRWM for color image denoising is also feasible. The basic idea is to first construct YUV color space by utilizing RGB three channels of noisy color image, and then employ MRWM in this paper to denoise Y component to obtain Y' component. Further, Y' component is merged with the original UV components to obtain $Y'UV$ space. Finally, the $Y'UV$ space is transferred back to RGB channels to get the restored image. Figure 10 shows two examples of color image denoising using this idea.

We utilize the two metrics EP and TP in [57] and [58] to evaluate the edge preservation and texture preservation of the denoised images respectively. Specifically, the edge preservation metric of the $m-th$ region of interest (ROI) in an image is defined as (19), shown at the bottom of the next page, where I_m and I'_m are the corresponding matrices

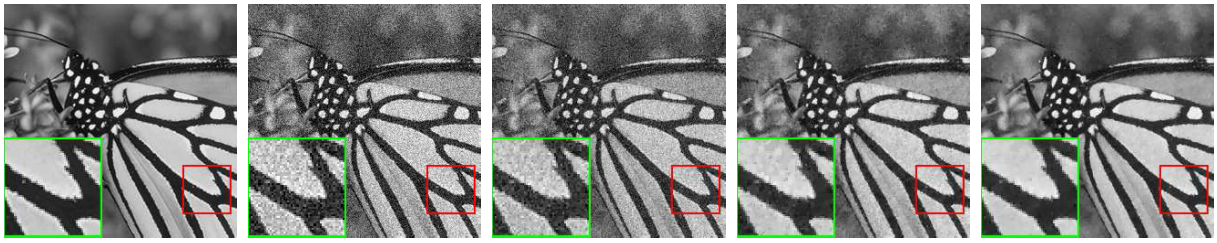

(a) Original image (b) Noisy image (c) MRWM-1 (22.85/0.5305) (d) MRWM-2 (25.87/0.7340) (e) MRWM-3 (**30.05/0.8763**)

FIGURE 6. Denoising visual comparison of MRWM-1, MRWM-2 and MRWM-3. One can see that MRWM-3 can yield the best visual effect.

TABLE 2. PSNR (dB) and SSIM comparison between MRWM and five competitive methods on the 12 test images shown in Figure 4. The highest index values have been bolded.

Images	1	2	3	4	5	6	7	8	9	10	11	12	Avg.
BM3D [18]	31.48	29.88	29.62	27.67	30.01	27.17	29.25	29.45	28.56	26.20	31.51	26.24	28.92
	0.8843	0.7770	0.8047	0.8306	0.8652	0.7119	0.8997	0.8544	0.8509	0.6865	0.8216	0.7100	0.8080
NCSR [20]	31.49	29.76	29.58	27.67	29.97	27.12	29.43	29.43	28.77	26.32	31.32	26.33	28.93
	0.8873	0.7718	0.8033	0.8265	0.8649	0.7016	0.9030	0.8570	0.8531	0.7004	0.8204	0.7173	0.8089
GHP [21]	31.47	29.76	29.61	27.73	29.95	27.19	29.22	29.42	28.72	26.32	31.24	26.37	28.92
	0.8812	0.7748	0.8033	0.8279	0.8616	0.7169	0.8943	0.8587	0.8516	0.7145	0.8151	0.7308	0.8109
WNNM [22]	31.73	29.99	29.77	28.07	30.19	27.41	29.85	29.64	29.03	26.34	31.48	26.38	29.16
	0.8871	0.7781	0.8078	0.8433	**0.8685**	0.7200	0.9089	**0.8600**	0.8579	0.7006	0.8223	0.7215	0.8147
W-LDMM [31]	31.81	29.90	29.74	28.18	30.05	27.58	29.92	29.43	29.01	26.88	31.68	26.57	29.23
	0.8251	0.7721	**0.8131**	0.8526	0.8302	**0.7721**	**0.9117**	0.8598	**0.8700**	0.7394	0.8224	0.7313	0.8167
MRWM	**31.83**	**30.12**	**30.11**	**29.42**	**30.46**	**27.70**	**30.05**	**30.10**	**29.60**	**27.85**	**32.48**	**28.23**	**29.83**
	0.8856	**0.7842**	0.8122	**0.8698**	0.8672	0.7420	0.8763	0.8200	0.8533	**0.7812**	**0.8408**	**0.8055**	**0.8282**

of the $m-th$ ROI in the original image and the denoised image respectively. Δ denotes a Laplacian operator. In fact, ΔI is a highpass filtered form of I. ΔI is acquired by a 3×3 pixel approximation of the Laplacian operator. $\bar{I}$ is the empirical mean of I. Γ represents the correlation within ROI:

$$\Gamma(I_1, I_2) = \sum_{(i,j)\in ROI} I_1(i,j)I_2(i,j). \tag{20}$$

Thus, the edge preservation on the M selected ROIs is expressed as

$$EP = \frac{1}{M}\sum_{m=1}^{M} EP_m. \tag{21}$$

One can find that EP has a larger value when the edge in ROI is sharp. On the other hand, texture preservation (TP) in a ROI is defined as

$$TP_m = \frac{\sigma_m^2}{(\sigma_m')^2}\sqrt{\frac{\mu_{ori}}{\mu_{den}}} \tag{22}$$

where σ_m^2 and $(\sigma_m')^2$ are the variance of the $m-th$ ROI in the original image and the denoised image respectively. μ_{ori} and μ_{den} are the corresponding mean values. Then the texture preservation over the M selected ROIs can be obtained

$$TP = \frac{1}{M}\sum_{m=1}^{M} TP_m. \tag{23}$$

It can be found that the larger the TP value, the better the texture preservation of the restored image.

Figure 11 shows regions of interest (ROI) of three images used for the evaluation of our EP and TP. Table 3 presents EP and TP evaluation results of three methods MRWM-1, MRWM-2 and MRWM-3 on three images Monarch, Cameraman and Starfish. It can be shown that in the proposed MRWM, the increase of the residual Wasserstein regularization term can effectively improve the performance of the restored images in edge and texture preservation.

Finally, we compare the proposed MRWM and multiple image denoising method t-SVD [59]. The 12 test images

$$EP_m = \frac{\Gamma(\Delta I_m' - \overline{\Delta I_m'}, \Delta I_m - \overline{\Delta I_m})}{\sqrt{\Gamma(\Delta I_m' - \overline{\Delta I_m'}, \Delta I_m' - \overline{\Delta I_m'})\Gamma(\Delta I_m - \overline{\Delta I_m}, \Delta I_m - \overline{\Delta I_m})}}, \tag{19}$$

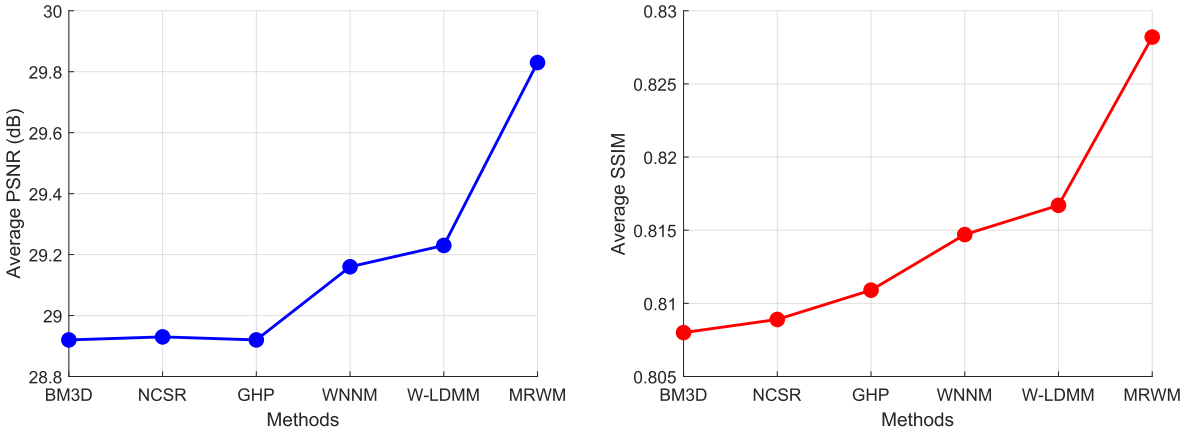

FIGURE 7. Average PSNR and SSIM curves of six denoising methods BM3D, NCSR, GHP, WNNM, W-LDMM and MRWM.

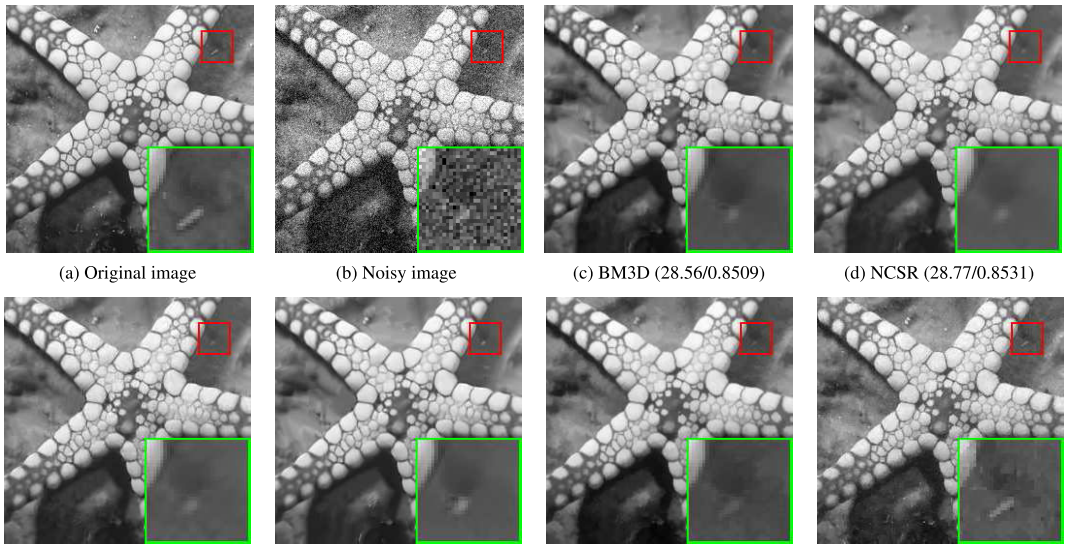

(a) Original image (b) Noisy image (c) BM3D (28.56/0.8509) (d) NCSR (28.77/0.8531)

(e) GHP (28.72/0.8516) (f) WNNM (29.03/0.8579) (g) W-LDMM (29.01/**0.8700**) (h) MRWM (**29.60**/0.8533)

FIGURE 8. Local visual magnification comparison for six image denoising methods. It can be found that the proposed MRWM can recover more image detail information, which makes the image look more natural.

TABLE 3. Edge preservation (EP) and texture preservation (TP) evaluation of three methods on three images.

Methods	Metrics	Monarch	Cameraman	Starfish
MRWM-1	EP	0.6768	0.6611	0.6004
	TP	0.9012	0.6632	0.8146
MRWM-2	EP	0.8236	0.8397	0.8949
	TP	0.9022	0.8618	0.8398
MRWM-3	EP	0.8580	0.9483	0.9203
	TP	0.9195	0.9743	0.9903

shown in Figure 4 are still employed for denoising comparison. Table 4 shows the results of corresponding Gaussian denoising experiments, including PSNR and SSIM index values. It can be found from Table 4 that in terms of PSNR, MRWM is superior to t-SVD on 12 images, and both methods have their own advantages in SSIM. But for the average values of the two metrics, MRWM outperforms t-SVD. Meanwhile, Figure 12 shows the enlarged local results of the two methods on test image 3. It can be found from Figure 12 that t-SVD tends to blur the edge details of the image, while the proposed MRWM can better recover the texture information of the image. Therefore, MRWM based on image prior regularization and multiple residual distribution constraints is effective in image denoising.

C. EXPERIMENTAL RESULTS ON THE DATASET BSD68

To show the denoising capacity of the proposed MRWM, on the basis of the original BM3D [18] and WNNM [22], we further employ three state-of-the-art methods, including the recent ATVBH [23], deep learning based methods DnCNN [36] and FFDNet [39]. Moreover, we use Berkeley

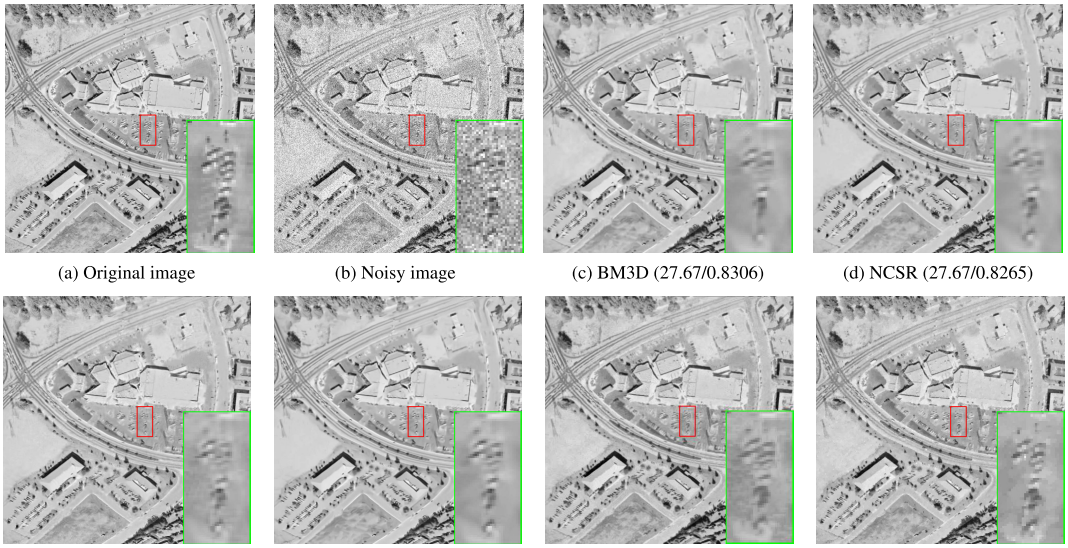

(a) Original image (b) Noisy image (c) BM3D (27.67/0.8306) (d) NCSR (27.67/0.8265)

(e) GHP (27.73/0.8279) (f) WNNM (28.07/0.8433) (g) W-LDMM (28.18/0.8526) (h) MRWM (**29.42/0.8698**)

FIGURE 9. **Local visual magnification comparison for six image denoising methods. One can see that MRWM has some advantages in preserving image detail features.**

(a) Original image (b) Noisy image (c) MRWM

FIGURE 10. **Examples of MRWM denoising on color images "Butterfly" and "Starfish" containing Gaussian noise with $\sigma = 25$.**

segmentation dataset (BSD68) [54] to test the Gaussian denoising performance of MRWM. The dataset BSD68 containing 68 natural images is widely utilized for the evaluation of Gaussian denoising methods. Table 5 shows the average PSNR and SSIM results of the six denoising methods on the dataset BSD68.

From Table 5, one can see that regarding the average PSNR and SSIM on BSD68, MRWM surpasses ATVBH by a large margin, and significantly outperforms BM3D and WNNM. According to the literature [60], [61], few denoising methods can exceed BM3D by more than 0.3dB on average. In contrast, the proposed MRWM outperforms BM3D by about 0.6dB for the average PSNR acting on the 68 images in BSD68. It should be mentioned that this gap (0.6dB) is very close to the PSNR bound (0.7dB) estimated over BM3D in [61].

It can also be found from Table 5 that the denoising effect of MRWM is slightly inferior to the deep learning based methods DnCNN and FFDNet. In fact, this is a common shortcoming of current model based denoising methods.

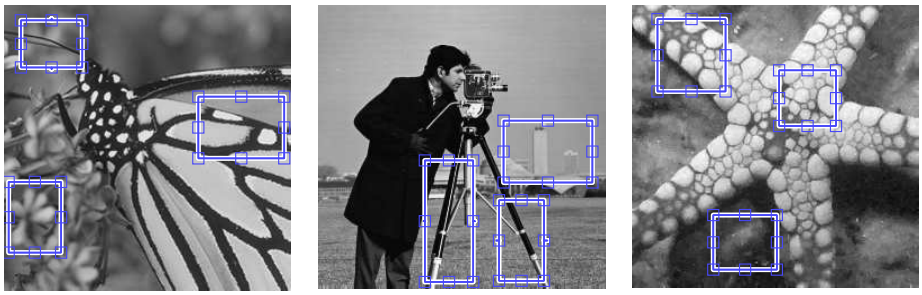

(a) Monarch (b) Cameraman (c) Starfish

FIGURE 11. Three regions of interest (ROI) of the images used for evaluation of edge preservation (EP) and texture preservation (TP).

TABLE 4. PSNR (dB) and SSIM comparison for our MRWM and t-SVD [59] on the 12 test images shown in Figure 4. The higher index values have been bolded.

Images	1	2	3	4	5	6	7	8	9	10	11	12	Avg.
t-SVD	30.56	28.94	28.31	27.50	29.62	27.59	28.83	28.43	28.39	25.06	30.62	25.89	28.31
	0.8880	**0.7930**	0.8060	0.8560	**0.8800**	**0.7600**	**0.9120**	**0.8430**	**0.8750**	0.7010	0.8320	0.7170	0.8219
MRWM	**31.83**	**30.12**	**30.11**	**29.42**	**30.46**	**27.70**	**30.05**	**30.10**	**29.60**	**27.85**	**32.48**	**28.23**	**29.83**
	0.8856	0.7842	**0.8122**	**0.8698**	0.8672	0.7420	0.8763	0.8200	0.8533	**0.7812**	**0.8408**	**0.8055**	**0.8282**

(a) Original image (b) Noisy image (c) t-SVD (28.31/0.8060) (d) MRWM (**30.11/0.8122**)

FIGURE 12. Local visual magnification comparison for the proposed MRWM and t-SVD [59]. One can see that t-SVD tends to blur the edge details of the image, while MRWM can restore the richer texture information.

TABLE 5. The average PSNR (dB) and SSIM of six denoising methods for noise level $\sigma = 25$ on the dataset BSD68 [54].

Dataset	Index	ATVBH [23]	BM3D [18]	WNNM [22]	DnCNN [36]	FFDNet [39]	MRWM
BSD68	PSNR	27.42	28.57	28.83	29.23	29.19	29.15
	SSIM	0.7628	0.8017	0.8088	0.8278	0.8289	0.8106

However, our experimental results show that MRWM outperforms DnCNN and FFDNet numerically and visually on some images of BSD68. Here, three examples of specific images are listed for discussion. Figure 13 illustrates the visual results of the six methods on the image "test001" in BSD68. It can be seen that ATVBH, BM3D, WNNM, DnCNN and FFDNet tend to polish the detailed texture on the original image. However, the proposed MRWM can recover more realistic texture information on the stone sculptures.

Figures 14-15 show the visual comparison results of the six methods on images "test008" and "test021" in BSD68 respectively. As can be seen from Figure 14, the tiger tail recovered by ATVBH, BM3D, WNNM, DnCNN and FFDNet is partially lost, while MRWM can better present the complete tiger tail. It can be found from Figure 15 that there are some white spots in the local part of the original image. ATVBH, BM3D, WNNM, DnCNN and FFDNet can only recover very few white point information, while MRWM can recover sufficient white point details, which is more consistent with the real characteristics of the image.

The above quantitative and qualitative evaluations on the dataset BSD68 confirm that the proposed MRWM can not only effectively remove noise, but also restore the detailed texture features of images. The Gaussian denoising

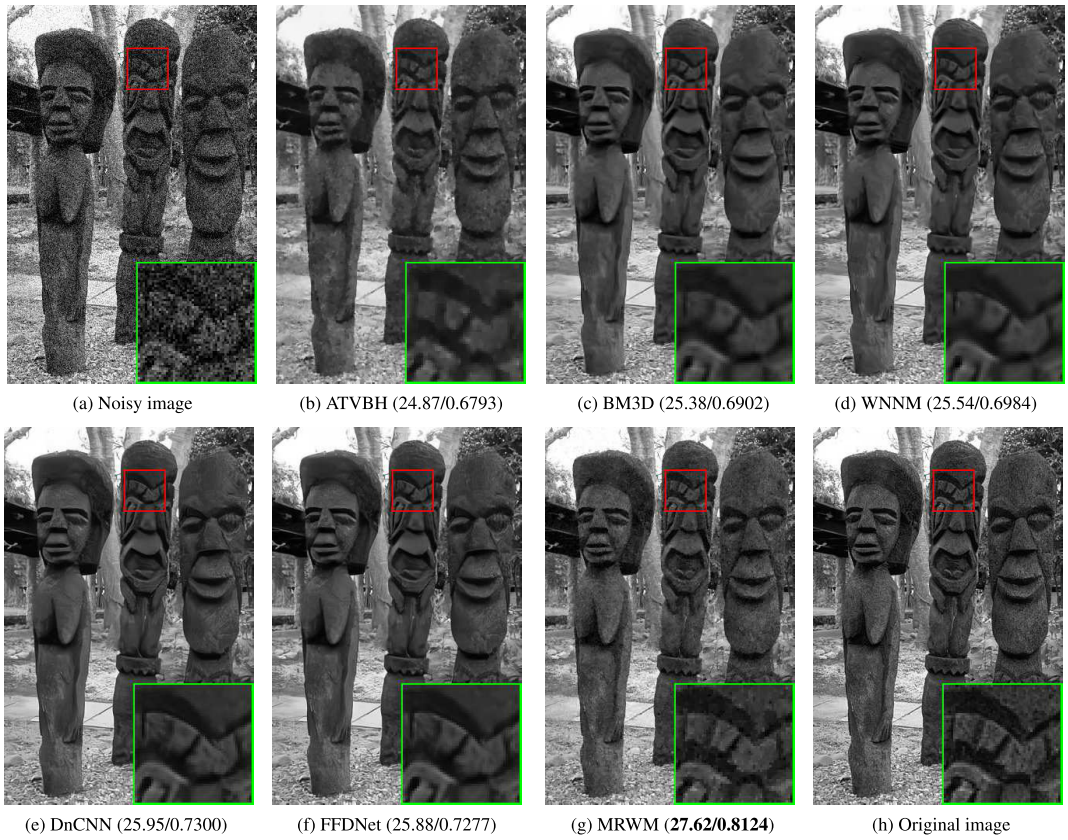

(a) Noisy image (b) ATVBH (24.87/0.6793) (c) BM3D (25.38/0.6902) (d) WNNM (25.54/0.6984)

(e) DnCNN (25.95/0.7300) (f) FFDNet (25.88/0.7277) (g) MRWM (**27.62/0.8124**) (h) Original image

FIGURE 13. Local visual magnification comparison of the image "test001" from the BSD68. One can see that MRWM can restore more realistic texture details of the original image.

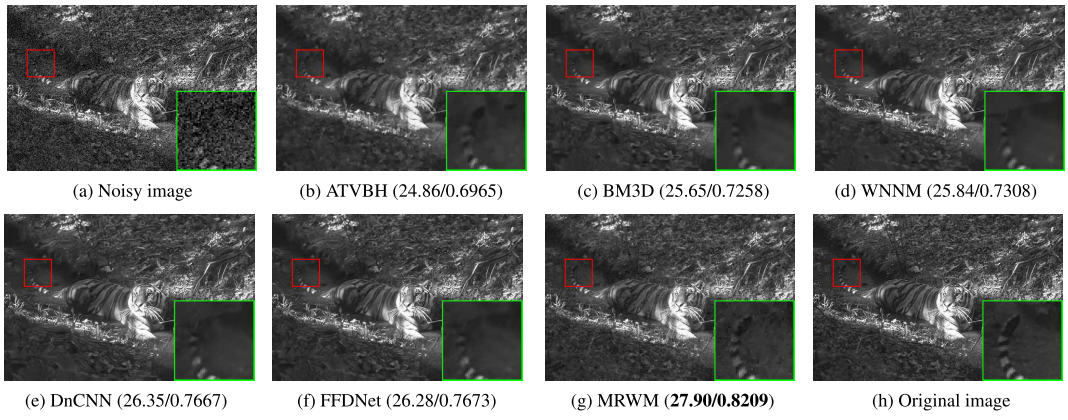

(a) Noisy image (b) ATVBH (24.86/0.6965) (c) BM3D (25.65/0.7258) (d) WNNM (25.84/0.7308)

(e) DnCNN (26.35/0.7667) (f) FFDNet (26.28/0.7673) (g) MRWM (**27.90/0.8209**) (h) Original image

FIGURE 14. Local visual magnification comparison of the image "test008" from the BSD68. It can be seen that MRWM can present the tiger's tail more completely.

performance obtained by MRWM is attributed to the combined effect of multiple residual Wasserstein distribution approximation and image prior regularization.

D. IMPLEMENTATION EFFICIENCY

In image denoising, in addition to the quality of image restoration, the implementation efficiency of denoising method also needs to be considered. Although deep learning based methods such as DnCNN and FFDNet require a short time in the testing phase, they often take a lot of time to train the required neural network. Moreover, such training generally has to rely on the GPU to complete. Here, an image of size 481 $\times$ 321 in BSD68 is taken as an example to illustrate the operating efficiency of the model based denoising methods. The running time of our MRWM (16s) is longer than that of BM3D (3s), but less than that of ATVBH (26s) and WNNM (601s). It should be noted that BM3D mainly implements image restoration through C language. Overall,

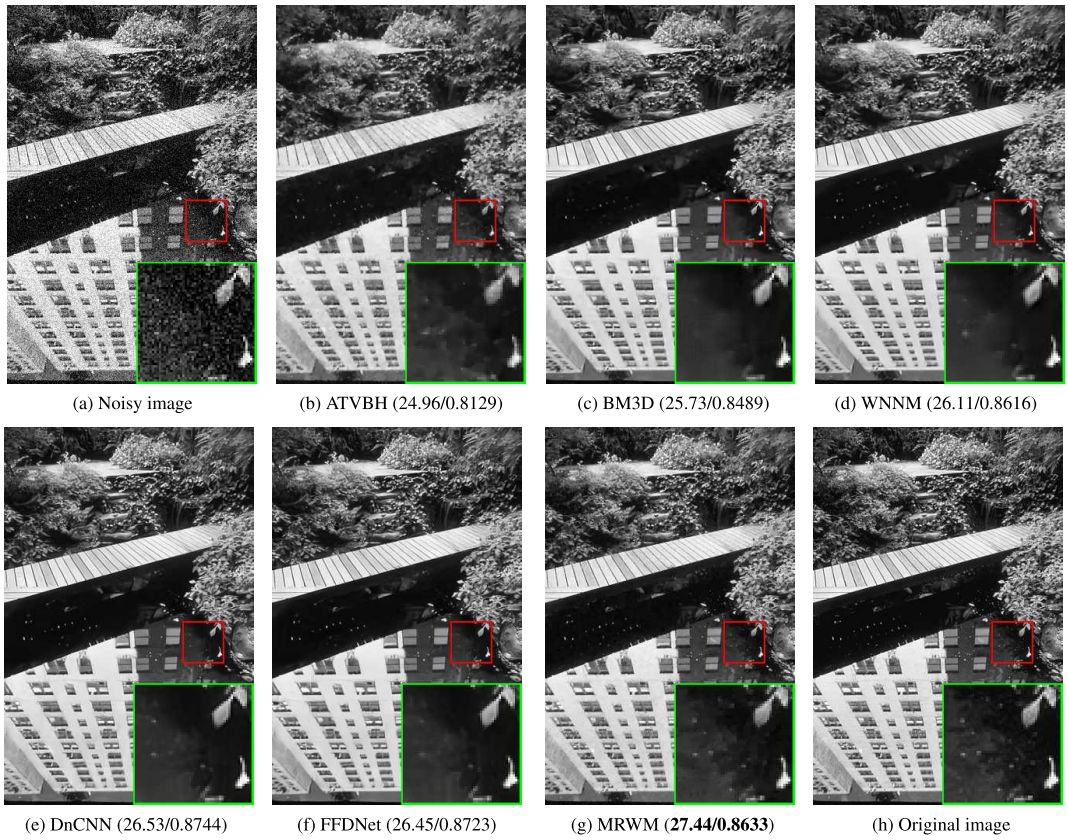

(a) Noisy image (b) ATVBH (24.96/0.8129) (c) BM3D (25.73/0.8489) (d) WNNM (26.11/0.8616)

(e) DnCNN (26.53/0.8744) (f) FFDNet (26.45/0.8723) (g) MRWM (**27.44/0.8633**) (h) Original image

FIGURE 15. Local visual magnification comparison of the image "test021" from the BSD68. It should be noted that MRWM can recover more abundant white dot information in the image.

MRWM is still competitive in the implementation efficiency of image denoising.

VII. CONCLUSION

Different from most model-based image denoising methods, which focus primarily on exploiting the physical prior information existing in the image itself, the core of the MRWM proposed in this paper is to mine the efficacy of the multiple residual distribution approximation of degraded images. The effective combination of the Wasserstein distance driven residual estimation and the image total variation prior contributes to the improvement of the image denoising effect. For this realistic and meaningful problem, the proposed MRWM algorithm is simple, but its image denoising performance is better. The multiple residual distribution approximation provides new ideas for the development of other image restoration tasks such as deblurring and inpainting.

A limitation of MRWM is that it cannot be directly applied to the removal of non-additive noise, such as multiplicative Poisson noise. The removal of non-additive noise has always been of interest and value. One strategy is to transform the degraded image into one with additive white Gaussian noise, and then make full use of MRWM for image restoration.

REFERENCES

[1] S. Osher, Z. Shi, and W. Zhu, "Low dimensional manifold model for image processing," *SIAM J. Imag. Sci.*, vol. 10, no. 4, pp. 1669–1690, Oct. 2017.

[2] X. Cao, X. Fu, C. Xu, and D. Meng, "Deep spatial–spectral global reasoning network for hyperspectral image denoising," *IEEE Trans. Geosci. Remote Sens.*, vol. 60, 2021, Art. no. 5504714.

[3] R. He, X. Feng, X. Zhu, H. Huang, and B. Wei, "RWRM: Residual Wasserstein regularization model for image restoration," *Inverse Problems Imag.*, vol. 15, no. 6, pp. 1307–1332, Dec. 2021.

[4] C. Zhao, X. Feng, X. Jia, R. He, and C. Xu, "Root-transformation based multiplicative denoising model and its statistical analysis," *Neurocomputing*, vol. 275, pp. 2666–2680, Jan. 2018.

[5] K. Zhang, W. Zuo, S. Gu, and L. Zhang, "Learning deep CNN denoiser prior for image restoration," in *Proc. IEEE Conf. Comput. Vis. Pattern Recognit. (CVPR)*, Jul. 2017, pp. 3929–3938.

[6] X. Jia, S. Liu, X. Feng, and L. Zhang, "FOCNet: A fractional optimal control network for image denoising," in *Proc. IEEE/CVF Conf. Comput. Vis. Pattern Recognit. (CVPR)*, Jun. 2019, pp. 6054–6063.

[7] Q. Ding, H. Ji, H. Gao, and X. Zhang, "Learnable multi-scale Fourier interpolation for sparse view CT image reconstruction," in *Proc. Int. Conf. Med. Image Comput. Comput.-Assist. Intervent (MICCAI)*, Sep. 2021, pp. 286–295.

[8] R. He, X. Feng, C. Zhao, H. Chen, X. Zhu, and C. Xu, "Image restoration based on adaptive dual-domain filtering," *Math. Problems Eng.*, vol. 2018, pp. 1–17, Oct. 2018.

[9] S. H. Chan, X. Wang, and O. A. Elgendy, "Plug-and-play admm for image restoration: Fixed-point convergence and applications," *IEEE Trans. Comput. Imag.*, vol. 3, no. 1, pp. 84–98, Jan. 2017.

[10] Q. Ding, H. Ji, Y. Quan, and X. Zhang, "A dataset-free deep learning method for low-dose CT image reconstruction," 2022, *arXiv:2205.00463*.

[11] H.-M. Zhang and B. Dong, "A review on deep learning in medical image reconstruction," *J. Oper. Res. Soc. China*, vol. 8, pp. 311–340, Jan. 2020.
[12] J. Mairal, F. Bach, J. Ponce, G. Sapiro, and A. Zisserman, "Non-local sparse models for image restoration," in *Proc. IEEE Int. Conf. Comput. Vis. (ICCV)*, Sep. 2009, pp. 2272–2279.
[13] M. Elad and M. Aharon, "Image denoising via sparse and redundant representations over learned dictionaries," *IEEE Trans. Image Process.*, vol. 15, no. 12, pp. 3736–3745, Dec. 2006.
[14] F. Fan, Y. Ma, C. Li, X. Mei, J. Huang, and J. Ma, "Hyperspectral image denoising with superpixel segmentation and low-rank representation," *Inf. Sci.*, vols. 397–398, pp. 48–68, Aug. 2017.
[15] J. Spiegelberg, J. C. Idrobo, A. Herklotz, T. Z. Ward, W. Zhou, and J. Rusz, "Local low rank denoising for enhanced atomic resolution imaging," *Ultramicroscopy*, vol. 187, pp. 34–42, Apr. 2018.
[16] H. Liu, R. Xiong, D. Liu, S. Ma, F. Wu, and W. Gao, "Image denoising via low rank regularization exploiting intra and inter patch correlation," *IEEE Trans. Circuits Syst. Video Technol.*, vol. 28, no. 12, pp. 3321–3332, Dec. 2018.
[17] Q. Ge, X. Jing, F. Wu, Z. Wei, L. Xiao, W. Shao, D. Yue, and H. Li, "Structure-based low-rank model with graph nuclear norm regularization for noise removal," *IEEE Trans. Image Process.*, vol. 26, no. 7, pp. 3098–3112, Jul. 2017.
[18] K. Dabov, A. Foi, V. Katkovnik, and K. Egiazarian, "Image denoising by sparse 3-D transform-domain collaborative filtering," *IEEE Trans. Image Process.*, vol. 16, no. 8, pp. 2080–2095, Aug. 2007.
[19] W. Dong, L. Zhang, and G. Shi, "Centralized sparse representation for image restoration," in *Proc. Int. Conf. Comput. Vis.*, Nov. 2011, pp. 1259–1266.
[20] W. Dong, L. Zhang, G. Shi, and X. Li, "Nonlocally centralized sparse representation for image restoration," *IEEE Trans. Image Process.*, vol. 22, no. 4, pp. 1620–1630, Apr. 2013.
[21] W. Zuo, L. Zhang, C. Song, D. Zhang, and H. Gao, "Gradient histogram estimation and preservation for texture enhanced image denoising," *IEEE Trans. Image Process.*, vol. 23, no. 6, pp. 2459–2472, Jun. 2014.
[22] S. Gu, Q. Xie, D. Meng, W. Zuo, X. Feng, and L. Zhang, "Weighted nuclear norm minimization and its applications to low level vision," *Int. J. Comput. Vis.*, vol. 121, no. 2, pp. 183–208, Jul. 2016.
[23] D. N. H. Thanh, V. B. S. Prasath, L. M. Hieu, and S. Dvoenko, "An adaptive method for image restoration based on high-order total variation and inverse gradient," *Signal, Image Video Process.*, vol. 14, no. 6, pp. 1189–1197, Feb. 2020.
[24] H. Liu, J. Zhang, and R. Xiong, "CAS: Correlation adaptive sparse modeling for image denoising," *IEEE Trans. Comput. Imag.*, vol. 7, pp. 638–647, 2021.
[25] N. N. Hien, D. N. H. Thanh, U. Erkan, and J. M. R. S. Tavares, "Image noise removal method based on thresholding and regularization techniques," *IEEE Access*, vol. 10, pp. 71584–71597, 2022.
[26] G. Carlsson, T. Ishkhanov, V. de Silva, and A. Zomorodian, "On the local behavior of spaces of natural images," *Int. J. Comput. Vis.*, vol. 76, no. 1, pp. 1–12, Jun. 2007.
[27] A. B. Lee, K. S. Pedersen, and D. Mumford, "The nonlinear statistics of high-contrast patches in natural images," *Int. J. Comput. Vis.*, vol. 54, no. 1, pp. 83–103, 2003.
[28] G. Peyre, "A review of adaptive image representations," *IEEE J. Sel. Topics Signal Process.*, vol. 5, no. 5, pp. 896–911, Sep. 2011.
[29] G. Peyré, "Manifold models for signals and images," *Comput. Vis. Image Understand.*, vol. 113, no. 2, pp. 249–260, 2009.
[30] Z. Shi, S. Osher, and W. Zhu, "Generalization of the weighted nonlocal Laplacian in low dimensional manifold model," *J. Sci. Comput.*, vol. 75, no. 2, pp. 638–656, Sep. 2017.
[31] R. He, X. Feng, W. Wang, X. Zhu, and C. Yang, "W-LDMM: A Wasserstein driven low-dimensional manifold model for noisy image restoration," *Neurocomputing*, vol. 371, pp. 108–123, Jan. 2020.
[32] F. Zhang, N. Cai, J. Wu, G. Cen, H. Wang, and X. Chen, "Image denoising method based on a deep convolution neural network," *IET Image Process.*, vol. 12, no. 4, pp. 485–493, Apr. 2018.
[33] W. Dong, P. Wang, W. Yin, and G. Shi, "Denoising prior driven deep neural network for image restoration," *IEEE Trans. Pattern Anal. Mach. Intell.*, vol. 41, no. 10, pp. 2305–2318, Oct. 2019.
[34] R. K. Vasudevan and S. Jesse, "Deep learning as a tool for image denoising and drift correction," *Microsc. Microanalysis*, vol. 25, no. S2, pp. 190–191, Aug. 2019.
[35] X. Mao, C. Shen, and Y. Yang, "Image restoration using very deep convolutional encoder–decoder networks with symmetric skip connections," in *Proc. Adv. Neural Inf. Process. Syst.*, Dec. 2016, pp. 2810–2818.
[36] K. Zhang, W. Zuo, Y. Chen, D. Meng, and L. Zhang, "Beyond a Gaussian denoiser: Residual learning of deep CNN for image denoising," *IEEE Trans. Image Process.*, vol. 26, no. 7, pp. 3142–3155, Jul. 2017.
[37] Y. Tai, J. Yang, X. Liu, and C. Xu, "MemNet: A persistent memory network for image restoration," in *Proc. IEEE Int. Conf. Comput. Vis. (ICCV)*, Oct. 2017, pp. 4539–4547.
[38] P. Liu, H. Zhang, K. Zhang, L. Lin, and W. Zuo, "Multi-level wavelet-CNN for image restoration," in *Proc. Comput. Vis. Pattern Recognit. (CVPR)*, Jun. 2018, pp. 773–782.
[39] K. Zhang, W. Zuo, and L. Zhang, "FFDNet: Toward a fast and flexible solution for CNN-based image denoising," *IEEE Trans. Image Process.*, vol. 27, no. 9, pp. 4608–4622, Sep. 2018.
[40] D. Valsesia, G. Fracastoro, and E. Magli, "Deep graph-convolutional image denoising," *IEEE Trans. Image Process.*, vol. 29, pp. 8226–8237, 2020.
[41] Y. Zhang, K. Li, K. Li, G. Sun, Y. Kong, and Y. Fu, "Accurate and fast image denoising via attention guided scaling," *IEEE Trans. Image Process.*, vol. 30, pp. 6255–6265, 2021.
[42] B. Fu, X. Zhang, L. Wang, Y. Ren, and D. N. H. Thanh, "Double enhanced residual network for biological image denoising," *Gene Expression Patterns*, vol. 45, Sep. 2022, Art. no. 119270.
[43] D. L. Donoho and J. M. Johnstone, "Ideal spatial adaptation by wavelet shrinkage," *Biometrika*, vol. 81, no. 3, pp. 425–455, 1994.
[44] A. Buades, Y. Lou, J. Morel, and Z. Tang, "Multi image noise estimation and denoising," HAL, Bengaluru, India, Tech. Rep. hal-00510866, Aug. 2010.
[45] X. Wang, K. Wu, Y. Zhang, Y. Xiao, and P. Xu, "A GAN-based denoising method for Chinese stele and rubbing calligraphic image," *Vis. Comput.*, vol. 32, no. 2, pp. 1–12, Feb. 2022.
[46] L. D. Tran, S. M. Nguyen, and M. Arai, "Gan-based noise model for denoising real images," in *Proc. Asian Conf. Comput. Vis.*, Nov. 2020, pp. 1–13.
[47] A. Alsaiari, R. Rustagi, A. Alhakamy, M. M. Thomas, and A. G. Forbes, "Image denoising using a generative adversarial network," in *Proc. IEEE 2nd Int. Conf. Inf. Comput. Technol. (ICICT)*, Mar. 2019, pp. 126–132.
[48] C. Villani, *Optimal Transport: Old and New*, vol. 338. Berlin, Germany: Springer, 2009.
[49] C. Solomon and T. Breckon, *Fundamentals of Digital Image Processing: A Practical Approach With Examples in MATLAB*. Hoboken, NJ, USA: Wiley, 2011.
[50] D. Zoran and Y. Weiss, "From learning models of natural image patches to whole image restoration," in *Proc. Int. Conf. Comput. Vis.*, Nov. 2011, pp. 479–486.
[51] D. Krishnan and R. Fergus, "Fast image deconvolution using hyperlaplacian priors," in *Proc. Adv. Neural Inf. Process. Syst.*, vol. 22, Dec. 2009, pp. 1–9.
[52] S. Park and J. Lim, "An overview of heavy-tail extensions of multivariate Gaussian distribution and their relations," *J. Appl. Statist.*, vol. 49, pp. 1–18, Mar. 2022.
[53] A. Chambolle, "An algorithm for total variation minimization and applications," *J. Math. Imag. Vis.*, vol. 20, no. 1, pp. 89–97, 2004.
[54] S. Roth and M. J. Black, "Fields of experts," *Int. J. Comput. Vis.*, vol. 82, no. 2, pp. 205–229, Apr. 2009.
[55] M. Wu, X. Jin, Q. Jiang, S.-J. Lee, W. Liang, G. Lin, and S. Yao, "Remote sensing image colorization using symmetrical multi-scale DCGAN in YUV color space," *Vis. Comput.*, vol. 37, no. 7, pp. 1707–1729, Aug. 2020.
[56] A. Zenati, W. Ouarda, and A. M. Alimi, "A new digital steganography system based on hiding online signature within document image data in YUV color space," *Multimedia Tools Appl.*, vol. 80, no. 12, pp. 18653–18676, Feb. 2021.
[57] F. Sattar, L. Floreby, G. Salomonsson, and B. Lövström, "Image enhancement based on a nonlinear multiscale method," *IEEE Trans. Image Process.*, vol. 6, no. 6, pp. 888–895, Jun. 1997.

[58] A. Pizurica, L. Jovanov, B. Huysmans, V. Zlokolica, P. D. Keyser, F. Dhaenens, and W. Philips, "Multiresolution denoising for optical coherence tomography: A review and evaluation," *Current Med. Imag.*, vol. 4, pp. 270–284, Nov. 2008.
[59] Z. Zhang, G. Ely, S. Aeron, N. Hao, and M. Kilmer, "Novel methods for multilinear data completion and de-noising based on tensor-SVD," in *Proc. IEEE Conf. Comput. Vis. Pattern Recognit.*, Jun. 2014, pp. 3842–3849.
[60] A. Levin and B. Nadler, "Natural image denoising: Optimality and inherent bounds," in *Proc. CVPR*, Jun. 2011, pp. 2833–2840.
[61] A. Levin, B. Nadler, F. Durand, and W. T. Freeman, "Patch complexity, finite pixel correlations and optimal denoising," in *Proc. IEEE Eur. Conf. Comput. Vis. (ECCV)*, Oct. 2012, pp. 73–86.

RUI-QIANG HE received the Ph.D. degree in applied mathematics from the School of Mathematics and Statistics, Xidian University, Xi'an, China, in 2020. He is currently working with the Mathematics Department, Xinzhou Teachers University, China. His research interests include inverse problems in image processing and mathematical models and algorithms for image processing.

WANG-SEN LAN received the M.S. degree from the Shanxi University of Finance and Economics, Taiyuan, China, in 2004. He is currently a Professor with the Mathematics Department, Xinzhou Teachers University, China. His research interests include data analysis and its application in image processing.

FANG LIU is currently pursuing the Ph.D. degree with the School of Science, North University of China. She is also an Associate Professor with the Mathematics Department, Xinzhou Teachers University, China. Her research interests include image processing, modeling, and simulation of complex systems.